

## Hydrothermal Synthesis of Flower-like Fe-doped VO<sub>2</sub>(B) with Enhanced Lithium Ion Storage Performance

Zhengguang Zou<sup>\*</sup>, Shichang Han, Yanwei Li, Xingyu Wu, Qian Yang, Tingting Lv

Key Laboratory of New Processing Technology for Nonferrous Metals and Materials of Ministry of Education, College of Material Science and Engineering, Guilin University of Technology, Guilin 541004, Guangxi, PR China

\*E-mail: [zouzgglut@163.com](mailto:zouzgglut@163.com)

Received: 14 April 2018 / Accepted: 15 May 2018 / Published: 5 July 2018

---

Flower-like Fe<sub>x</sub>VO<sub>2</sub>(B) samples (x=0-0.045mol%) have been successfully fabricated via a hydrothermal method followed with annealing in argon atmosphere at 350°C for 1 h. The physical properties of the prepared samples were analyzed by XRD, XPS, FESEM, and EDS analyses. The electrochemical properties of the prepared samples were characterized by cyclic voltammetry(CV), electrochemical impedance spectroscopy (EIS), and charge-discharge tests. The results demonstrated that Fe doping could enhance the electrochemical reaction reversibility, decrease charge transfer resistance, and increase the specific capacity of VO<sub>2</sub>(B). In particular, the Fe<sub>0.03</sub>VO<sub>2</sub>(B) sample showed the best lithium storage performance with initial discharge capacity of 306 mAh g<sup>-1</sup> at the current density of 0.1 C in the voltage range from 1.5 to 4.0 V, much higher than that (195 mAh g<sup>-1</sup>) of the pure VO<sub>2</sub>(B).

---

**Keywords:** lithium-ion batteries; electrochemical performance; VO<sub>2</sub>(B); Fe doping; hydrothermal method

### 1. INTRODUCTION

The ever-increasing demand for electric vehicles (EV) and renewable energy sources (wind, water, and solar energy) is pushing the development of high performance energy storage and conversion devices. Lithium-ion batteries (LIBs) are currently considered as one of the most popular energy storage devices due to the advantages of their high-energy density, high-rate capability, relatively low self-discharge rate, and high energy density[1-6]. However, it still a great challenge for LIBs to meet the requirements for applications in the fields of EV and large-scale stationary (“grid”) energy storage. Among various potential cathode materials for the next-generation LIBs, vanadium oxides (V<sub>2</sub>O<sub>5</sub>, V<sub>6</sub>O<sub>13</sub>, VO<sub>2</sub>, V<sub>2</sub>O<sub>3</sub>, etc.) have attracted more and more attentions because of their

distinct advantages of high specific capacity, abundant sources, and low cost [7-17]. In particular, VO<sub>2</sub> (B) stand out for LIBs due to its large theoretical capacity (320 mAh g<sup>-1</sup>) [18] and unique bilayer structure with abundant tunnels for fast Li<sup>+</sup> intercalation/deintercalations[19-21]. Unfortunately, the practical application of VO<sub>2</sub> (B) as cathode material of LIBs has been hampered due to its slow electrochemical kinetics, low electronic and ionic conductivity, and poor structural stability[22]. One of the ways to surmount these drawbacks is to carry out transition elements doping, such as Cu<sup>2+</sup>, Al<sup>3+</sup> and Ti<sup>4+</sup>[23,24].

Herein, we report a Fe-doped VO<sub>2</sub>(B) material with flower-like morphology prepared by using a facile hydrothermal method. The effect of Fe doping on the microstructure and electrochemical performance of VO<sub>2</sub>(B) are investigated in detail. The results demonstrate that Fe doping could significantly enhance the lithium storage performance of VO<sub>2</sub>(B).

## 2. MATERIALS AND METHODS

### 2.1. Synthesis of Fe doping VO<sub>2</sub>(B)

Fe-doped VO<sub>2</sub>(B) were synthesized by a facile hydrothermal method. All chemical reagents were analytical grade and used without further purification. In a typical synthesis procedure, 1.25 g oxalic acid dihydrate (C<sub>2</sub>H<sub>2</sub>O<sub>4</sub>·2H<sub>2</sub>O) and 0.4g Vanadium pentoxide (V<sub>2</sub>O<sub>5</sub>) were dissolved in 20 mL of deionized water. The mixed solution was kept under constant stirring at 80°C in a water bath until a blue colored VO<sub>2</sub>C<sub>2</sub>O<sub>4</sub> solution formed, and then a suitable amount of Fe(NO<sub>3</sub>)<sub>3</sub>·9H<sub>2</sub>O, 20ml of the VO<sub>2</sub>C<sub>2</sub>O<sub>4</sub> solution and 3 ml of 30% H<sub>2</sub>O<sub>2</sub> were added into a 100 ml Inner lining of reaction kettle pre-filled with 30 ml of deionized water. After stirring for 10 minutes, the autoclave was sealed and maintained at 160°C for 24 h in an oven, followed by natural cooling to room temperature. After the hydrothermal reaction, the resultant precipitate was collected by filtration, washed with deionized water several times, and then freeze dried to get the precursor. Finally, the obtained precursor was annealed in nitrogen atmosphere at 350°C for 1 h to obtain the Fe-doped VO<sub>2</sub>(B). The molar ratios of Fe to V were increased gradually from 0% to 4.5% and the corresponding samples were labeled as pure VO<sub>2</sub>(B), Fe<sub>0.015</sub>VO<sub>2</sub>(B), Fe<sub>0.03</sub>VO<sub>2</sub>(B), and Fe<sub>0.045</sub>VO<sub>2</sub>(B).

### 2.2. Characterization

All the samples were characterized by using a Philips X'pert Pro diffractometer with a Cu K $\alpha$  radiation source ( $\lambda = 0.154$  nm) at the scanning rate of 6 °/min. Scanning electron microscopy (SEM) images were recorded on a Hitachi S-4800 field emission scanning electron microscopy. X-ray photoelectron spectroscopy (XPS) measurements were carried out with an ESCALAB 250Xi spectrometer using a Al K $\alpha$  (1486.6eV) X-ray source. All spectra were calibrated to the binding energy of the C 1s peak at 284.8 eV. The base pressure was around 10<sup>-8</sup> Pa.

### 2.3. Electrochemical measurements

The electrochemical performances of the Fe-VO<sub>2</sub>(B) samples were investigated in two electrode coin-type cells (CR2025) that were assembled in a glove box. Filled with ultrahigh-purity argon. Fe-VO<sub>2</sub>(B), acetylene black, and polyvinylidene fluoride (PVDF) binder in a weight ratio of 7:2:1 were mixed and then dispersed in N-methyl-2-pyrrolidone (NMP) solvent to make a slurry, which was then coated uniformly on Al foil and dried in a vacuum oven at 90°C for 12 h to obtain the cathodes. 1 mol/L LiPF<sub>6</sub> dissolved in a mixture of dimethyl carbonate (DMC), ethylene carbonate (EC) and diethyl carbonate (DEC) was used as the electrolyte (DMC/EC/DEC=2:2:1 in volume). Lithium metal was employed as the counter and reference electrodes, and Celgard 2400 was used as the separator. Galvanostatic charge/discharge measurements were performed using a multichannel battery testing system (NEWARE CT3008W). Electrochemical impedance spectroscopy (EIS) and cyclic voltammetry (CV) were tested using a CHI760D electrochemical workstation.

## 3. RESULTS AND DISCUSSION

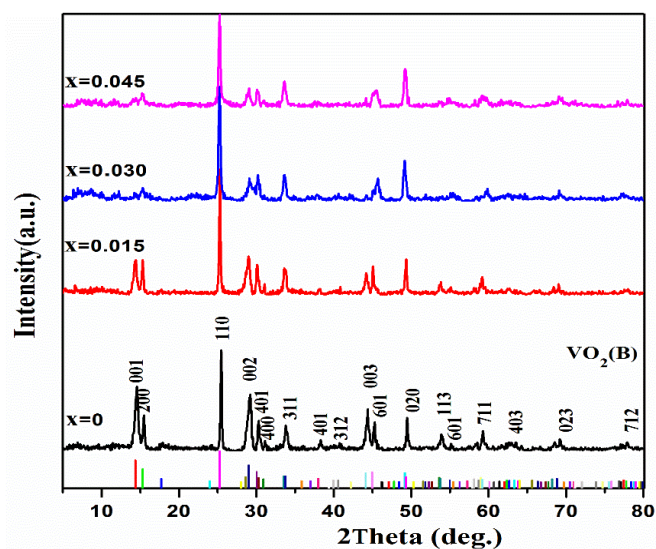


**Figure 1.** XRD patterns of the series of Fe-VO<sub>2</sub>(B) samples.

Figure 1 shows the XRD patterns of the pure VO<sub>2</sub>(B) and Fe-doped VO<sub>2</sub>(B) samples. The peaks from all the samples show a single monoclinic VO<sub>2</sub> phase (JCPDS Card No.81-2392) and no impurity phase is detected [25], suggesting that Fe doping has no effect on the phase structure of VO<sub>2</sub>(B). However, with the increase of Fe content, the (001) diffraction peak decreases gradually. Table 1 compares the lattice parameters of the pure VO<sub>2</sub>(B) and Fe-doped VO<sub>2</sub>(B) samples. The lattice parameters were determined by using the MDI Jade software (Jade 6 XRD Pattern Processing Software). Obviously, the interlayer distance (*c*) increases with the increase of Fe doping content, which can be due to the larger ionic radius of Fe<sup>3+</sup> (0.65 Å) than that of V<sup>4+</sup> (0.58 Å) [26,27].

**Table 1.** Comparison of the lattice parameters and cell volume for the series of Fe-VO<sub>2</sub>(B) samples.

Specimen	<i>a</i> (Å)	<i>b</i> (Å)	<i>c</i> (Å)	<i>V</i> (Å <sup>3</sup> )
VO <sub>2</sub> (B)	12.0396	3.6737	6.4199	271.79
Fe <sub>0.015</sub> VO <sub>2</sub>	12.0684	3.6833	6.4321	274.17
Fe <sub>0.030</sub> VO <sub>2</sub>	12.0010	3.7042	6.4593	274.51
Fe <sub>0.045</sub> VO <sub>2</sub>	12.0649	3.6968	6.4613	275.22

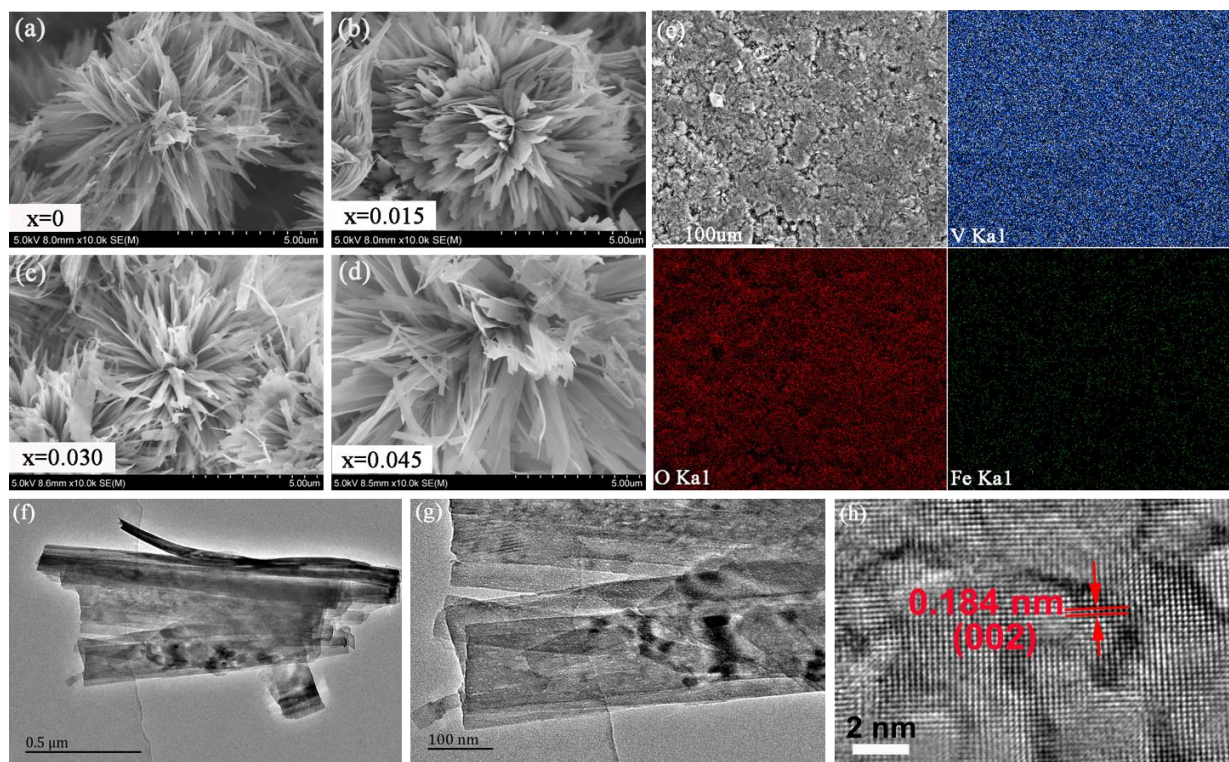
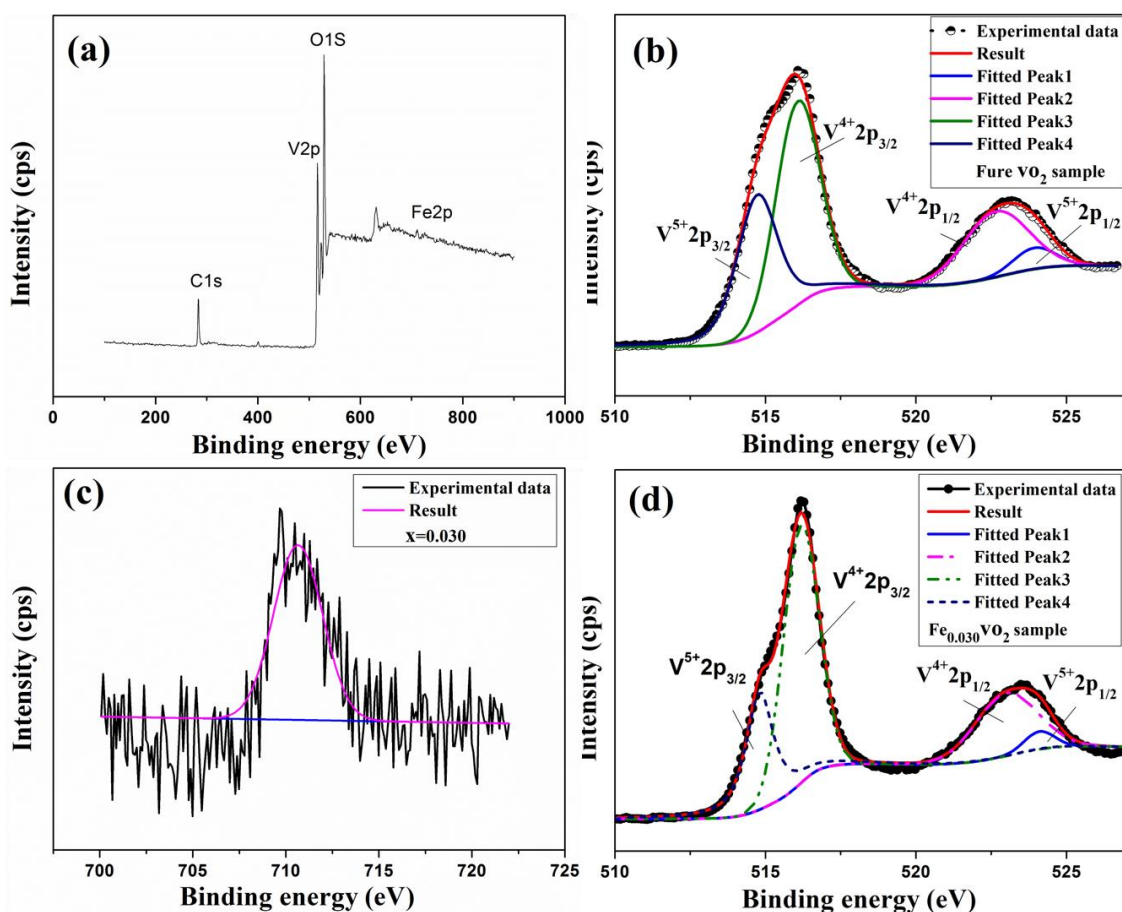
**Figure 2.** (a-d) FESEM images of the series of Fe-VO<sub>2</sub>(B) samples; (e) element mapping images of V, O, and Fe of Fe<sub>0.030</sub>VO<sub>2</sub>(B); (f-g) TEM images of Fe<sub>0.030</sub>VO<sub>2</sub>(B); (h) HRTEM image of Fe<sub>0.030</sub>VO<sub>2</sub>(B).

Fig. 2 (a-d) presents the FESEM images of the series of Fe-doped VO<sub>2</sub>(B) samples. It can be clearly seen that all the four samples exhibit hierarchical flower-like microspheres morphologies, which are composed of end-connected nanosheets. There are plenty of structural voids between the primary building blocks, which is beneficial for electrode/electrolyte contact and enhances the kinetics performance. Meanwhile this special structure was also beneficial to the transport of Li<sup>+</sup>. By a detail observation, one can find that the lateral size of the nanosheets increases with the increase of Fe doping content. The Sheet width of VO<sub>2</sub>(B) is about 150nm observed from the TEM image (Fig. 2g), which is in accordance with the FESEM image. The high resolution TEM (HRTEM) image shown in Fig. 2h bring out the clear lattice fringes of the Fe<sub>0.030</sub>VO<sub>2</sub>(B) with lattice interplanar spacing of 0.184 nm, which corresponding to the (002) crystal plane of VO<sub>2</sub>(B) and is in good agreement with the XRD results. Table 2 gives molar ratio of Fe to V in the series of Fe-VO<sub>2</sub>(B) samples estimated from EDS

analysis.

**Table 2.** The molar ratio of iron to vanadium in the series of Fe-VO<sub>2</sub>(B) samples.

Specimen	mass ratio	mol ratio
VO <sub>2</sub> (B)	0	0
Fe <sub>0.015</sub> VO <sub>2</sub>	0.012	0.013
Fe <sub>0.030</sub> VO <sub>2</sub>	0.030	0.038
Fe <sub>0.045</sub> VO <sub>2</sub>	0.047	0.052



**Figure 3.** (a) XPS survey spectrum of the Fe<sub>0.030</sub>VO<sub>2</sub>(B) sample; (b) high-resolution spectrum of V 2p core-level spectrum for pure VO<sub>2</sub>(B) sample; (c) high-resolution spectrum of Fe 2p core-level spectrum for Fe<sub>0.030</sub>VO<sub>2</sub>(B) sample; (d) high-resolution spectrum of V 2p core-level spectrum for Fe<sub>0.030</sub>VO<sub>2</sub>(B) sample.

XPS were carried out on the pure VO<sub>2</sub>(B) and Fe-doped VO<sub>2</sub>(B) samples to investigate chemical information such as the oxidation state, and the results are shown in Fig. 3. The binding energy appeared at 514.68, 516.03, 522.69 and 523.95eV in the sample of pure VO<sub>2</sub>(B) could be assigned to V<sup>5+</sup> 2p<sub>3/2</sub>, V<sup>4+</sup> 2p<sub>3/2</sub>, V<sup>5+</sup> 2p<sub>1/2</sub> and V<sup>4+</sup> 2p<sub>1/2</sub> peaks, respectively[28-32]. Meanwhile, these four binding energy values also existed in the Fe<sub>0.030</sub>VO<sub>2</sub>(B) sample. It indicates that the iron atoms are successfully doped into the VO<sub>2</sub>(B). Meanwhile, Energy dispersive X-ray spectroscopic element

mapping analysis (Fig. 2 (e-h)) indicates that Fe, V and O uniformly distributed in the microparticles. It is confirmed that the  $\text{Fe}^{3+}$  is uniformly doped in  $\text{VO}_2(\text{B})$  (Fig.2 (e-h)).

However, the  $\text{V}^{5+} 2p_{3/2}$  concentration in the Fe-doped  $\text{VO}_2(\text{B})$  sample is much lower than that in the pure  $\text{VO}_2(\text{B})$  sample. Therefore, Fe doping contributes to the formation of low valence state vanadium in  $\text{VO}_2(\text{B})$ . Maybe it's because  $\text{Fe}^{3+}$  replace the site of  $\text{V}^{5+}$ . For the Fe-doped  $\text{VO}_2(\text{B})$  sample, Fe element is displayed with sharp photoelectron peaks at binding energies of 710.56 eV (Fig.3c). This agrees well with the reported data of  $\text{Fe}^{3+} 2p_{3/2}$  in  $\text{VO}_2(\text{B})$ [33] indicating that the Fe atoms in Fe-doped  $\text{VO}_2(\text{B})$  sample primarily exist in the form of  $\text{Fe}^{3+}$  ions.

**Table 3.** Comparison of the lithium storage performance of the Fe doping  $\text{VO}_2(\text{B})$  to reported cathode materials.

Samples	Current density (mA $\text{g}^{-1}$ )	Capacity retention (mA h $\text{g}^{-1}$ )	Ref.
Fe-doped $\text{VO}_2(\text{B})$	32.4	198 after 100 cycles	This work
Al-doped $\text{VO}_2(\text{B})$	32.4	202 after 50 cycles	[23]
Cu-doped $\text{VO}_2(\text{B})$	42	234 after 51 cycles	[24]
Ti-doped $\text{VO}_2(\text{B})$	42	217 after 51 cycles	[24]

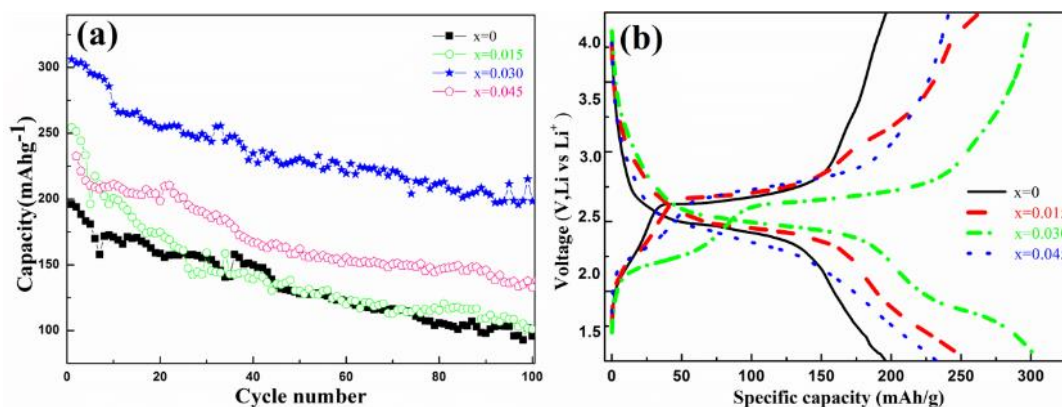


**Figure 4.** (a) Cycling performance of the pure  $\text{VO}_2(\text{B})$  and Fe-doped  $\text{VO}_2(x=0.015, 0.030, 0.045)$  samples at 0.1C discharge-charge rate; (b) Initial charge-discharge profiles of the samples at 0.1C in the voltage range of 1.5-4.0V.

Fig. 4a gives the cycling performance of the pure  $\text{VO}_2(\text{B})$  and Fe-doped  $\text{VO}_2(x=0.015, 0.030, 0.045)$  samples under a current density of 0.1C (32.4 mA  $\text{g}^{-1}$ ). It can be seen from Figure 4 that the  $\text{Fe}_{0.03}\text{VO}_2(\text{B})$  sample shows the highest lithium storage activity. For example, the initial discharge capacities of the  $\text{Fe}_{0.03}\text{VO}_2(\text{B})$  sample is 306 mA h  $\text{g}^{-1}$ , which is much higher than that (195 mA h  $\text{g}^{-1}$ ) of the pure  $\text{VO}_2(\text{B})$ . After 100 cycles, the specific capacity of the  $\text{Fe}_{0.03}\text{VO}_2(\text{B})$  sample stabilized at 198 mA h  $\text{g}^{-1}$ , while the specific capacity of pure  $\text{VO}_2(\text{B})$  is only 95 mA h  $\text{g}^{-1}$ . The cycling stability are much superior to the previous reported cathode vanadium oxide materials (as listed in Table 3).

Fig. 4b showed the first charge-discharge curves of the pure VO<sub>2</sub>(B) and Fe-doped VO<sub>2</sub> samples at the current density of 0.1 C. All of them show a distinct charge platform at about 2.7 V and a distinct discharge platform at about 2.5V, which are agreement with that of the reference [7, 34, 35]. The results suggested that appropriate Fe<sup>3+</sup> doping could significantly improve the lithium storage performance of VO<sub>2</sub>(B). This performance enhancement can be due to the expansion of interlayer space resulting from Fe<sup>3+</sup> doping as illustrating in Table 1[36].

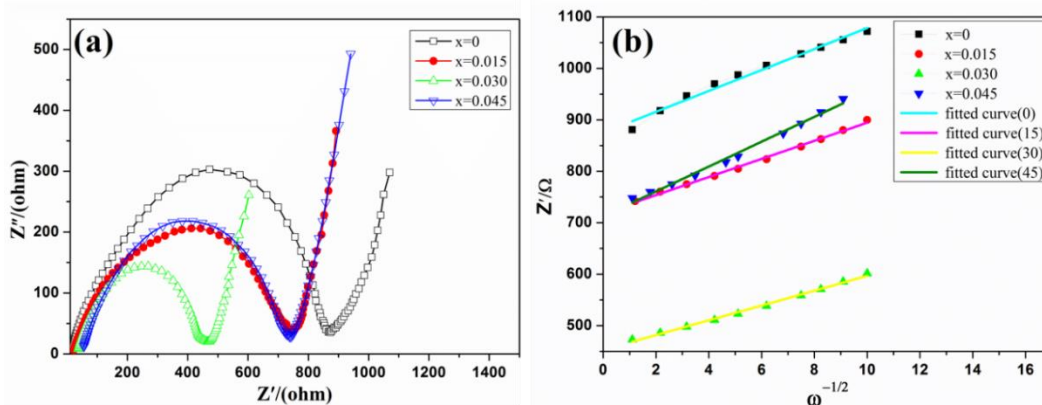


**Figure 5.** (a) Nyquist plots of the pure VO<sub>2</sub>(B) and Fe<sub>x</sub>VO<sub>2</sub> (x=0.015, 0.030, 0.045) electrodes; (b) The relationship between  $Z'$  and  $\omega^{-1/2}$  at low frequencies.

**Table 4.**  $R_s$  and  $R_{ct}$  values of pristine VO<sub>2</sub> (B) and Fe<sup>3+</sup> doped VO<sub>2</sub>(B) products.

Specimen	$R_s$ ( $\Omega$ )	$R_{ct}$ ( $\Omega$ )
VO <sub>2</sub>	11	889.7
Fe <sub>0.015</sub> VO <sub>2</sub>	17.37	736.5
Fe <sub>0.030</sub> VO <sub>2</sub>	33.34	414.9
Fe <sub>0.045</sub> VO <sub>2</sub>	49.63	692.9

To further explore the influence of Fe<sup>3+</sup> doping on electrochemical property, EIS spectra are measured at the 1<sup>th</sup> fully discharged state and the Nyquist plots are shown in Figure 6. In the equivalent circuit diagram,  $R_s$  is the electrolyte resistance;  $R_{ct}$  is the charge-transfer resistance, which can be calculated by the diameter of the semicircle; W is the Warburg impedance related to the diffusion process of lithium-ions into the bulk of the electrode materials; CPE is employed to consider the porosity and tortuosity characteristics of the electrode. Table 4 gives the simulated  $R_s$  and  $R_{ct}$  values of the four electrodes. It can be seen that the pure VO<sub>2</sub>(B) electrode shows a  $R_{ct}$  value of 889.7  $\Omega$ . After Fe<sup>3+</sup> doping, the  $R_{ct}$  value decreases and in particular the Fe-doped VO<sub>2</sub>(x=0.030) electrode exhibit the smallest  $R_{ct}$  value of 414.9  $\Omega$ , which is only about half of that for the pure VO<sub>2</sub>(B). This result indicates that the Fe<sup>3+</sup> doping makes the electrochemical reaction in VO<sub>2</sub>(B) proceeds more easily.

The Li<sup>+</sup> diffusion coefficients (D) in the Fe-doped VO<sub>2</sub> samples are also estimated according to the following equation[37]:

$$D_{Li} = \frac{R^2 T^2}{2A^2 n^4 F^4 C^2 \sigma_w^2} \tag{1}$$

where  $R$  is the gas constant,  $T$  is the absolute temperature,  $A$  is the surface area of the anode,  $n$  is the number of electrons per molecule during cycling,  $F$  is Faraday constant,  $C$  is the concentration of lithium ion,  $\sigma_w$  is the Warburg factor which can be obtained from the following equation[38]:

$$Z' = R_s + R_{ct} + \sigma_w \omega^{-1/2} \quad (2)$$

where  $R_s$  is the resistance of the electrolyte and electrode material,  $R_{ct}$  is the charge transfer resistance and  $\omega$  is the angular frequency in the low frequency region. The relationship plot between  $Z'$  and  $\omega^{-1/2}$  at low frequency region is shown in Fig. 6b. According to Eqs. (1) and (2), the  $\text{Li}^+$  diffusion coefficient of the Fe-doped  $\text{VO}_2(\text{B})$  samples ( $x=0, 0.015, 0.030, 0.045$ ) is  $8.04 \times 10^{-15} \text{ cm}^2 \text{ s}^{-1}$ ,  $1.07 \times 10^{-14} \text{ cm}^2 \text{ s}^{-1}$ ,  $1.61 \times 10^{-14} \text{ cm}^2 \text{ s}^{-1}$  and  $5.65 \times 10^{-15} \text{ cm}^2 \text{ s}^{-1}$ , respectively. With the increasing of doping concentration, the lithium diffusion coefficient firstly increases and then decreases and the sample of  $\text{Fe}_{0.030}\text{VO}_2(\text{B})$  has the maximum  $D_{\text{Li}}$ . It indicates that a proper amount of  $\text{Fe}^{3+}$  doping is beneficial to the diffusion of lithium ions.

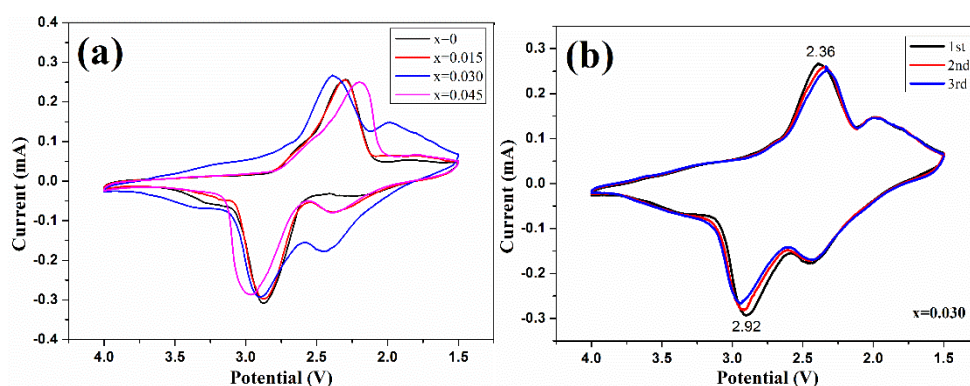


**Figure 6.** (a) Comparison of the first CV cycles of the pure  $\text{VO}_2(\text{B})$  and Fe-doped  $\text{VO}_2(\text{B})$  samples at a sweep rate of  $0.1 \text{ mV s}^{-1}$ ; (b) CV curves of the  $\text{Fe}_{0.030}\text{VO}_2(\text{B})$  electrode at a scan rate of  $0.1 \text{ mV s}^{-1}$ .

Furthermore, the first cycle CV curves of the pure  $\text{VO}_2(\text{B})$  and Fe-doped  $\text{VO}_2(\text{B})$  samples are investigated at a sweep rate of  $0.1 \text{ mV s}^{-1}$  in the potential range from 1.5 to 4.0 V (Fig. 7a). The four samples exhibit similar CV features: in the first scan, an obvious reduction peak centered at 2.4 V can be observed in the discharge process, and meanwhile, corresponding oxidation peak at 2.9 V can be observed in the charging process. The redox peak potentials were in accordance with the literature [39].

Owing to the potential difference reflects the polarization degree of the electrode and the encapsulated area of the cathodic scan reflects battery capacity[40]. By comparison, we have found that the  $\text{Fe}_{0.030}\text{VO}_2(\text{B})$  sample exhibits the largest curve area, least polarization, and highest redox currents among the four samples. The results indicate that the  $\text{Fe}_{0.030}\text{VO}_2(\text{B})$  present the highest electrochemical reaction activity and the best electrochemical reaction reversibility. Fig. 7b presents the CV curves of the  $\text{Fe}_{0.030}\text{VO}_2(\text{B})$  electrode for the first three CV cycles at a sweep rate of  $0.1 \text{ mV s}^{-1}$  from 1.5 to 4.0 V. Its cyclic voltammetry (CV) peak positions and intact areas retain almost invariant in the first three cycles, indicating excellent electrochemical reversibility and superior cycling stability of the  $\text{Fe}_{0.030}\text{VO}_2(\text{B})$  electrode.

#### 4. CONCLUSIONS

In summary, Fe-doped VO<sub>2</sub>(B) samples have been synthesized by a hydrothermal process following with annealing at 350 °C for 1 h in nitrogen. The as-prepared samples exhibit hierarchical flower-like microsphere morphologies, which are composed of end-connected nanosheets. Fe doping expand interlayer distance and increase the V<sup>4+</sup>/ V<sup>5+</sup> ratio of VO<sub>2</sub>(B). The Fe-doped VO<sub>2</sub>(B) samples exhibit higher reversible capacity, lower electrochemical reaction resistance, and higher electrochemical reversibility as compared to the pure VO<sub>2</sub>(B). In particular, the Fe<sub>0.03</sub>VO<sub>2</sub>(B) sample showed the best lithium storage performance with initial discharge capacity of 306 mAh g<sup>-1</sup> when recorded at the current density of 0.1C in the voltage range of 1.5 to 4.0 V, much higher than that (195 mAh g<sup>-1</sup>) of the pure VO<sub>2</sub>(B). According to the results, the improve lithium storage performance may attributed to the increased interlay distance of VO<sub>2</sub>(B), which facilitates lithium ion fast migration in VO<sub>2</sub>(B) during charge/discharge process. Moreover, the substitution of Fe<sup>3+</sup> to V<sup>4+</sup> in VO<sub>2</sub>(B) can form Fe–O–V bonds, which could stabilize the VO<sub>6</sub> octahedras, and therefore improve the cycling performance.

#### ACKNOWLEDGEMENTS

This work is financially supported by the National Science Foundation of China (No. 51562006).

#### References

1. D. Larcher, J.M. Tarascon, *Nat. Chem.*, 7 (2014) 19.
2. Z. Yang, J. Zhang, M.C. Kintner-Meyer, X. Lu, D. Choi, J.P. Lemmon and J. Liu, *Chem. Rev.*, 111 (2011) 3577.
3. J Yan , H. Fang, X. Jia and L.Wang, *Journal of Alloys and Compounds*, 730 (2018) 103.
4. N.S. Choi , Z. Chen , S.A. Freunberger, X. Ji , Y.K. Sun , K. Amine , G. Yushin, L.F. Nazar, J. Cho and P.G. Bruce, *Angew. Chem. Int. Ed.*, 51 (2012) 9994.
5. A.S. Hameed, M.V. Reddy, M. Nagarathinam, T. Runčevski and R.E. Dinnebier, *Scientific Reports*, 5 (2015) 16270.
6. C.K. Chan, H. Peng , G. Liu, K.M. Wrath, X.F. Zhang, R.A. Huggins and Y. Cui, *Nature Nanotechnology*, 3 (2008) 187.
7. C.V.S. Reddy, E.H.W. Jr, S.A.W. Sr, Q.L. Williams and R.R. Kalluru, *Current applied physics*, 9 (2009) 1195.
8. Q. Zhao, L. Jiao, W. Peng, H. Gao, J. Yang, Q. Wang, H. Du, L. Li, Z. Qi, Y. Si, Y. Wang and H. Yuan, *J. Power Sources*, 199 (2012) 350.
9. A. M. Cao, J. S. Hu, H. P. Liang and L. J. Wan, *Angew. Chem. Int. Ed.*, 44 (2005) 4391.
10. Y. Wang, G. Cao , *Chem. Mater.*, 18 (2006) 2787.
11. J. Livage, *Chemistry of Materials*, 3 (1991) 578.
12. M. D. Wei, H. Sugihara, I. Honma, M. Ichihara and H. S. Zhou, *Adv. Mater.*, 17 (2005) 2964.
13. A. Odani, V.G. Pol, S.V. Pol, M. Koltypin, A. Gedanken and D. Aurbach, *Adv. Mater.*, 18 (2006) 1431.
14. C. Tsang, A. Manthiram, *J. Electrochem. So.*, 144 (1997) 520.

15. F.J. Quites, H.O. Pastore, *Materials Research Bulletin*, 45 (2010) 892.
16. D. M. Rojas, E. Baudrin, *Solid State Ionics*, 178 (2007) 1268.
17. C.L. Onnerud, J.O. Thomas, M. Hardgrave and S.Y. Anderson, *J. Electrochem. Soc.*, 142 (1995) 3648.
18. E. Baudrin, G. Sudant, D. Larcher, B. Dunn and J.M. Tarascon, *Aerogels. Chem. Mater.*, 18 (2006) 4369.
19. H. Li, P. He, Y. Wang, E. Hosono and H. Zhou, *J. Mater. Chem.*, 21 (2011) 10999.
20. L. Mao, C. Liu and Mater.Res. Bull, *Materials Research Bulletin*, 43 (2008) 1384.
21. S.R. Popuri, M. Miclau, A. Artemenko, C. Labrugere, A. Villesuzanne and M. Pollet, *Inorg. Chem.*, 52 (2013) 4780.
22. H. Liu, Y. Wang, K. Wang, E. Hosono and H. Zhou, *J. Mater. Chem.*, 19 (2009) 2835.
23. Z.G. Zou, Z.L. Hou, J.L. Wang, Y. Gao, Z.D. Wan and S.C. Han, *Int. J. Electrochem. Sci.*, 12 (2017) 4979.
24. H. Cheng, Dissertation, China, Guilin University of Technology (2014).
25. J. Liu, Q. Li, T.Wang, D. Yu and Y. Li, *Angew. Chem. Int. Ed.*, 43 (2004) 5048.
26. F. Lin, W. Shi and A. Liu, *Journal of Alloys & Compounds*, 529 (2012) 21.
27. A. Aguadero, C.D.L. Calle, J.A. Alonso, D. Pérez-Coll, M.J. Escudero and L. Daza, *J. Power Sources*, 192 (2009) 78.
28. X.H. Liu, G.Y. Xie, C. Huang, Q. Xu, Y.F. Zhang and Y.B. Luo, *Materials Letters*, 62 (2008) 1878.
29. Q. Ni, Y. Bai, Z. Yang, Y. Li, G.H. Chen, L.M. Ling, H.X. Ren, S. Chen, F. Wu and C. Wu, *J. Alloy. Compd.*, 729 (2017) 49.
30. X.Y. Chen, X. Wang, Z.H. Wang and Y.T. Qian, *Nanotechnology*, 15 (2004) 1685.
31. Q.H. Wu, A. Thissen and W. Jaegermann, *Applied Surface Science*, 250 (2005) 57.
32. L.L. Liu, X.J. Wang, Y.S. Zhu, C.L. Hu, Y.P. Wu and R. Holze, *Journal of Power Sources*, 224 (2013) 290.
33. Y.X. Wang, W.Z. Liang, W. Huang and M. Gao, Y. Zhang, *Journal of Materials Science: Materials in Electronics*, 27 (2016) 6382.
34. Z.J. Chen, S.K. Gao, L.L. Jiang, C.L. Hu, Y.P. Wu and R. Holze, *Mater. Chem. Phys.*, 121 (2010) 254.
35. F. Sediri, F. Touati and N. Gharbi, *Materials Science & Engineering B*, 129 (2006) 251.
36. K. Lu, X. Liu, H. Zhang and Z.Q. Hu, *Acta Metallurgica Sinica*, 31 (1995) 74.
37. S.B. Ni, X.H. Lv, J.J. Ma, X.L. Yang and L.L. Zhang, *J. Power Sources*, 2014 (270) 564.
38. X.H. Rui, N. Ding, J. Liu, C. Li and C.H. Chen, *Electrochim. Acta.*, 55 (2010) 2384.
39. M. M. Rahman, J. Z. Wang, N. H. Idris, Z. X. Chen and H. K. Liu, *Electrochim. Acta*, 56 (2010) 693.
40. H.P. Liu, G.W. Wen, S.F. Bi, C.Y. Wang, J.M. Hao and P. Gao, *Electrochim. Acta*, 192 (2016) 38.